1 New Methodology Shows Short Atmospheric Lifetimes of

2 Oxidized Sulfur and Nitrogen due to Dry Deposition

3 Katherine Hayden[1], Shao-Meng Li[1,2*], Paul Makar[1], John Liggio[1], Samar G. Moussa[1], Ayodeji
4 Akingunola[1], Robert McLaren[3], Ralf M. Staebler[1], Andrea Darlington[1], Jason O'Brien[1], Junhua
5 Zhang[1], Mengistu Wolde[4], Leiming Zhang[1]

6 [1]*Air Quality Research Division, Environment and Climate Change Canada, Toronto, Ontario,*
7 *Canada, M3H 5T4*

8 [2]*College of Environmental Science and Engineering, Peking University, Beijing 100871 China*

9 [3]*Center for Atmospheric Chemistry, York University, 4700 Keele Street, Toronto, Ontario,*
10 *Canada*

11 [4]*National Research Council Canada, Flight Research Laboratory, Ottawa, Canada K1A 0R6*

12 *corresponding authors shaomeng.li@pku.edu.cn; Katherine.hayden@canada.ca

14 Abstract

16 The atmospheric lifetimes of pollutants determine their impacts on human health, ecosystems
17 and climate and yet, pollutant lifetimes due to dry deposition over large regions have not been
18 determined from measurements. Here, a new methodology based on aircraft observations is used
19 to determine the lifetimes of oxidized sulfur and nitrogen due to dry deposition over $(3\text{-}6)\times10^3$
20 km^2 of boreal forest in Canada. Dry deposition fluxes decreased exponentially with distance
21 resulting in lifetimes of 2.2-26 hours. Fluxes were 2-14 and 1-18 times higher than model
22 estimates for oxidized sulfur and nitrogen, respectively, indicating dry deposition velocities
23 which were 1.2-5.4 times higher than those computed for models. A Monte-Carlo analysis with
24 five commonly used inferential dry deposition algorithms indicates that such model
25 underestimates of dry deposition velocity are typical. These findings indicate that deposition to
26 vegetation surfaces are likely under-estimated in regional and global chemical transport models
27 regardless of the model algorithm used. The model-observation gaps may be reduced if surface
28 pH, and quasi-laminar and aerodynamic resistances in algorithms are optimized as shown in the
29 Monte-Carlo analysis. Assessing the air quality and climate impacts of atmospheric pollutants
30 on regional and global scales requires improved measurement-based understanding of
31 atmospheric lifetimes of these pollutants.

1 Introduction

Deposition represents the terminating process for most air pollutants and the starting

point for ecosystem impacts. Understanding deposition is critical in determining the atmospheric

lifetimes and spatial scale of atmospheric transport of pollutants, which in turn, dictates their

ecosystem (WHO, 2016; Solomon et al., 2007) and climate (Samset et al., 2014) impacts. In

particular, atmospheric lifetimes (τ) of oxidized sulfur and nitrogen compounds influence their

concentrations and column burdens in air, which affect air quality and hence human exposure

(WHO, 2016). Furthermore, the lifetime of these species affects their contributions to

atmospheric aerosols, with a consequent influence on climate via changes to radiative transfer

through scattering and cloud formation (Solomon et al., 2007). In addition, their deposition can

exceed critical load thresholds causing aquatic and terrestrial acidification, and eutrophication in

the case of nitrogen deposition (Howarth, 2008; Bobbink et al., 2010; Doney, 2010; Vet et al.,

2014; Wright et al., 2018). Quantifying τ and deposition thus provides a crucial assessment of

these regional and global impacts.

Deposition occurs through wet and dry processes. While wet deposition fluxes can be

measured directly (Vet et al., 2014), there are few validated methods for dry deposition fluxes

(Wesley and Hicks, 2000), and none which estimates deposition over large regions. Dry

deposition fluxes (F) may be obtained using micrometeorological measurements for pollutants

for which fast response instruments are available. However, these results are only valid for the

footprints of the observation sites, typically hundreds of meters (Aubinet e al., 2012), and their

extrapolation to larger regions may suffer from representativeness issues. As a result,

atmospheric lifetimes τ with respect to dry deposition have not been determined through direct

observations. On a regional scale, dry deposition fluxes are typically derived by multiplying

56 network-measured or model-predicted air concentrations with dry deposition velocities (V_d)

57 (Sickles and Shadwick, 2015; Fowler et al., 2009; Meyers et al., 1991), which are derived using

58 resistance-based inferential dry deposition algorithms (Wu et al., 2018), and compared with

59 limited micrometeorological flux measurements (Wesley and Hicks, 2000; Wu et al., 2018;

60 Finkelstein et al., 2000; Matsuda et al., 2006; Makar et al., 2018) for validation. When applied to

61 a regional scale, an inferential-algorithm derived V_d may have significant uncertainties (Wesley

62 and Hicks, 2000; Aubinet et al., 2012;Wu et al., 2018; Finkelstein et al., 2000; Matsuda et al.,

63 2006; Makar et al., 2018; Brook et al., 1997). For example, inferred V_d for SO_2, despite being

64 the most studied and best estimated, may be underestimated by 35% for forest canopies

65 (Finkelstein et al., 2000). Underestimated V_d for SO_2 and nitrogen oxides can contribute to

66 model over-prediction of regional and global SO_2 concentrations (Solomon et al., 2007; Christian

67 et al., 2015; Chin et al., 2000), or under-prediction of global oxidized nitrogen dry deposition

68 fluxes (Paulot et al., 2018; Dentener et al., 2006).

69 Here, a new approach is presented to determine τ with respect to dry deposition and F for

70 total oxidized sulfur (**TOS**, the sulfur mass in SO_2 and particle-SO_4 (pSO_4)) and total reactive

71 oxidized nitrogen (**TON**, the nitrogen mass in NO, NO_2, and others designated as NO_z) on a

72 spatial scale of (3-6)x10^3 km^2, using aircraft measurements. This approach provides a unique

73 methodology to determine τ and F over a large region. Coupled with analyses for chemical

74 reaction rates (for **TOS** compounds), the average V_d for **TOS** and **TON** over the same spatial

75 scale were also determined. The airborne measurements were obtained during an intensive

76 campaign from August to September 2013 in the AOSR (Gordon et al., 2015; Liggio et al., 2016;

77 Li et al., 2017; Baray et al., 2018; Liggio et al., 2019) in northern Alberta, Canada. Direct

78   comparisons with modelled dry deposition estimates are made to assess their uncertainties and

79   the spatial-temporal scales of air pollutant impacts.

80   **2 Methods**

81   **2.1 Lagrangian Flight Design**

82   Details of the airborne measurement program have been described elsewhere (Gordon et

83   al., 2015; Liggio et al., 2016; Li et al., 2017; Liggio et al., 2019; Baray et al., 2018). Briefly, an

84   instrumented National Research Council of Canada's Convair-580 research aircraft was flown

85   over the Athabasca oil sands region (AOSR) in Alberta, Canada from August 13 to September 7,

86   2013. The flights were designed to determine emissions, assess atmospheric transformation

87   processes and gather data for satellite and numerical model validation. Three flights were flown

88   to study transformation and deposition processes by flying a Lagrangian pattern so that the same

89   pollutant air mass was sampled at different time intervals downwind of emission sources for a

90   total of 4-5 hrs. Flights 7 (F7, Aug 19), 19 (F19, Sep 4) and 20 (F20, Sep 5) took place during

91   the afternoon when the boundary layer was well established. The flights were conducted in clear

92   sky conditions so wet deposition processes were insignificant. The aircraft flew tracks

93   perpendicular to the plume at multiple altitudes between 150 to 1400 m agl and multiple

94   intercepts of the plume downwind. Vertical profiles conducted as spirals were flown at the

95   centre of the plume which provided information on the boundary layer height and extent of

96   plume mixing. There were no other anthropogenic sources downwind of the AOSR.

97   **2.2 Aircraft Measurements**

98   A comprehensive suite of detailed gas- and particle-phase measurements were made from

99   the aircraft. Measurements pertaining to the analysis in this paper are discussed below.

100   **SO₂ and NOy.** Ambient air was drawn in through a 6.35 mm (1/4”) diameter PFA sampling line

101   taken from a rear-facing inlet located on the roof towards the rear of the aircraft. The inlet was

102   pressure-controlled to 770 mm Hg using a combination of a MKS pressure controller and a

103   Teflon pump.   Ambient air from the pressure-controlled inlet was fed to instrumentation for

104   measuring SO_2 and NO_y. SO_2 was detected via pulsed fluorescence with a Thermo 43iTLE

105   (Thermo Fisher Scientific, Franklin, MA, USA). NO_y (also denoted as Total Oxidized Nitrogen

106   (TON)) was measured by passing ambient air across a heated (325ºC) molybdenum converter

107   that reduces reactive nitrogen oxide species to NO. NO was then detected through

108   chemiluminescence with a Thermo 42iTL (Thermo Fisher Scientific). An inlet filter was used

109   for SO_2, but NO_y includes particulate nitrate (pNO_3), NO, NO_2, HNO_3 and other oxides of

110   nitrogen such as peroxy acetyl nitrate. The conversion efficiency of the heated molybdenum

111   converter and inlet transmission was evaluated with NO_2 and HNO_3 and found to be near 100%

112   and >90%, respectively.   Other NO_y species are expected to be greater than that of HNO_3.

113   Species like NO_3 radical and N_2O_5 are expected to be low as they photolyze quickly during

114   daytime. Zeros were performed 3-5 times per flight for all instruments by passing ambient air

115   through an in-line Koby King Jr cartridge for ~5 minutes. Multiple calibrations were conducted

116   before, during and after the study using National Institute Standards and Technology reference

117   standards. Data were recorded at a time resolution of 1 second and corrected for a sampling time

118   delay of 1-3 seconds depending on the instrument.

119   **Aerosols.** Multiple aerosol instruments sub-sampled from a forward facing, shrouded, isokinetic

120   particle inlet (Droplet Measurement Technologies, Boulder, CO, USA). A Time-of-Flight High

121   Resolution Aerosol Mass Spectrometer (AMS) (Aerodyne Research Inc.) was used to measure

122   non-refractory submicron aerosol components including pSO_4, pNO_3, pNH_4, and p-organics.

123   Details of the AMS and its operations have been published elsewhere (DeCarlo et al., 2006).

124   The instrument was operated in mass spectrometry V-mode with a time resolution of 10 seconds.

125   Filtered measurements were taken 4-5 times per flight to determine background signals.

126   Ionization efficiency calibrations using monodisperse ammonium nitrate were performed during

127   the study with an uncertainty of ±9%. Data were corrected for a sampling time delay of 10

128   seconds by comparing with faster response instruments e.g. a wing-mounted Forward Scattering

129   Spectrometer Probe Model 300 (FSSP-300) and an in-board Ultra High Sensitivity Absorption

130   Spectrometer (UHSAS) (both from Droplet Measurement Technologies). The AMS data were

131   processed using AMS data analysis software (Squirrel, version 1.51H and PIKA, version 1.10H).

132   A collection efficiency was applied to the data and determined by comparing the total AMS-

133   derived mass with the mass derived from the size distribution measurements from the UHSAS

134   assuming a density based on the chemical composition; the collection efficiency ranged from 0.5

135   to 1.

136   Measurements are discussed in terms of total oxidized sulfur (TOS, the sulfur mass in

137   SO_2 and particle-SO_4 (pSO_4)) and total reactive oxidized nitrogen (TON, the nitrogen mass in

138   reactive oxidized nitrogen species, often denoted NO_y).

139   **Volatile Organic Compounds (VOCs).** Selected VOCs were used to estimate the OH

140   concentrations used for determining oxidation rates for SO_2. VOCs were measured with a proton

141   transfer reaction time-of-flight mass spectrometer (PTR-ToF-MS, Ionicon Analytik GmbH,

142   Austria) as well as through discrete canister grab samples. The PTR-ToF-MS and its operation,

143   along with the details of the canister sampling and lab analyses during the study were described

144   in detail previously (Li et al., 2017). Briefly, the PTR-ToF-MS used chemical ionization with

145   H_3O^+ as the primary reagent ion. Gases with a proton affinity greater than that of water were

146   protonated in the drift tube. The pressure and temperature of the drift tube region were

147   maintained at a constant 2.15 mbar and 60°C, respectively for an E/N of 141 Td. The protonated

148   gases were detected using a high-resolution time of flight mass spectrometer at a time resolution

149   of 2 seconds. Instrumental backgrounds were performed in flight using a custom-built zero-air

150   generating unit. The unit contained a catalytic converter heated to 350°C with a continuous flow

151   of ambient air at a flow rate of one litre per minute. The data were processed using Tofware

152   software (Tofwerk AG). Calibrations were performed on the ground using gas standard mixtures

153   from Ionicon, Apel-Reimer and Scott-Marrin for 22 compounds. The canister samples were

154   collected in pre-cleaned and passivated 3L stainless steel canisters that were subsequently sent to

155   an analytical laboratory for GC-FID/MS analyses for a suite of 150 hydrocarbon compounds.

156   **Meteorology and aircraft state parameters.** Meteorological measurements have been

157   described elsewhere (Gordon et al., 2015). In brief, 3-D wind speed and temperature were

158   measured with a Rosemount 858 probe. Dew point was measured with an Edgetech hygrometer

159   and pressure was measured with a DigiQuartz sensor. Aircraft state parameters including

160   positions and altitudes were measured with GPS and a Honeywell HG1700 unit.

161

162   **2.3 Mass transfer rates in the atmosphere**

163   Mass transfer rates (T) across flight screens (Figure 1) were determined using an

164   extension of the Top-down Emission Rate Retrieval Algorithm (TERRA) developed for emission

165   rate determination using aircraft measurements (Gordon et al., 2015). Briefly, at each plume

166   interception location, the level flight tracks were stacked to create a virtual screen.   Background

167   subtracted pollutant concentrations and horizontal wind speeds normal to the screen were

168   interpolated using kriging. The background for SO_2 was ~0 ppb and pSO_4 was $0.2 - 0.3 \, \mu g \, m^{-3}$

169   which was subtracted from the pSO4 measurements before mass transfer rates were calculated

170   (Liggio et al., 2016). Integration of the horizontal fluxes across the plume extent on the screen

171   yields the transfer rate T. Using SO2 as an example,

172    $$T_{SO_2} = \int_{s_1}^{s_2} \int_{z_1}^{z_2} C(s,z) u_n(s,z) ds dz \qquad\qquad (1)$$

173   where $C(s,z)$ is the background subtracted concentration at screen coordinate s and z, which

174   represent the horizontal and vertical axes of the screen. The $u_n(s,z)$ is the horizontal wind speed

175   normal to the screen at the same coordinates.

176   Since the lowest flight altitude was 150 magl, it was necessary to extrapolate the data to

177   the surface as per the procedures described previously (Gordon et al., 2015). Extrapolation to the

178   surface methods were compared and differences were included in the uncertainty estimates.

179   Since the main source of SO2 is from the elevated facility stacks, the uncertainty for a single

180   screen is estimated at 4% (Gordon et al., 2015). NOy was also extrapolated linearly to the

181   surface and the mass transfer rates were similarly compared to other extrapolation methods. NOy

182   sources include the elevated facility stacks and surface sources such as the heavy hauler trucks

183   operating in the surface mines. The uncertainty in the resulting T for a single screen is estimated

184   to be larger at 8%, as a larger fraction of the NOy mass may be below the lowest measurement

185   altitude (Gordon et al., 2015). Sulfur and nitrogen data were also extrapolated linearly to

186   background values from the highest altitude flight tracks upwards to the mixed layer height,

187   which was determined from vertical profiles of pollutant mixing ratios, temperature and dew

188   point (Table 1). Two different approaches, a finite jump model and a gradient flux approach

189   (Stull, 1988; Degrazia et al., 2015), were used to estimate the potential upward loss across the

190   interface between the boundary layer and the free troposphere for sulfur. In both approaches, the

191   upward S flux was a minor loss at < 45 g/km^2/hr, about 3 orders of magnitude lower than the

192   several to many kg/km^2/hr horizontal advectional transport that were determined using TERRA.

193   Changes in T (denoted ΔT) were then calculated as the differences in T between pairs of

194   virtual screens. The uncertainty in ΔT was estimated as 8% for **TOS** and 26% for **TON** as

195   supported by emission rate uncertainties determined for box flights (Gordon et al., 2015). The

196   uncertainty analysis for box flights is applicable to ΔT here, as both account for uncertainties

197   with an upwind and a downwind screen. The ΔT uncertainties were propagated through

198   subsequent calculations.

199   Knowing ΔT, and accounting for the net rates of chemical loss and formation between

200   screens for SO$_2$ and pSO$_4$, the deposition rates (and subsequently the deposition flux in tonnes S

201   (or N) km^{-2} hr^{-1}, Section 2.4 were determined as follows, using sulfur compounds as an example:

202    $$\Delta T_{SO_2} = T_{SO_2}(t_2) - T_{SO_2}(t_1) = X_{SO2} - D_{SO2} \qquad (2)$$

203    $$\Delta T_{pSO_4} = T_{pSO_4}(t_2) - T_{pSO4}(t_1) = X_{pSO4} - D_{pSO4} \qquad (3)$$

204    $$\Delta T_{TOS} = T_{TOS}(t_2) - T_{TOS}(t_1) = -D_{TOS} \qquad (4)$$

205   where X_{SO2} is the rate of chemical reaction loss of sulfur mass in SO$_2$, X_{pSO4} is the rate of

206   chemical formation of sulfur mass as pSO$_4$, D_{SO2} and D_{pSO4} are deposition rates of sulfur mass in

207   SO$_2$ and pSO$_4$ respectively, and t_1 and t_2 are plume interceptions times at Screen 1 and Screen 2,

208   respectively. Reaction with the OH radical was considered to be the most significant chemical

209   loss of SO$_2$ and the most significant path for the formation of pSO$_4$ (further details in SI Section

210   S4. X_{SO2} and X_{pSO4} were determined using estimated OH radical concentrations, which were

211   determined using the methodology described in SI Section S4.

212   Dry deposition rates, D_{SO2} and D_{pSO4}, and their uncertainties were determined using Eq.

213   (2) and (3). For total oxidized sulfur **TOS** (i.e., sulfur in SO_2 + pSO_4) and total oxidized

214   nitrogen **TON** (i.e., nitrogen in NO_y) the chemistry term is not relevant, and thus, the dry

215   deposition rate D_{TOS} was directly determined from ΔT_{TOS} using equation (4), and respectively for

216   **TON**.

217

2.4 Dry deposition fluxes and dry deposition velocities

219   Average dry deposition fluxes (F) for **TOS** and **TON** were obtained by dividing the

220   deposition rates D with the footprint surface area of the plume between two adjacent screens

221   (Figure 1 grey shaded regions), as shown in Equation 5 for the dry deposition flux F_{TOS} of **TOS**

222   (in t S km^2 hr^{-1}):

223    $$F_{TOS} = \frac{D_{TOS}}{Area} \qquad\qquad (5)$$

224   where the surface area, *Area*, was identified as the geographic area under the plume extending to

225   the edges of the plume where concentrations fell to background levels (i.e. SO_2 to ~0 ppb; SO_4

226   ~0.2 ug m^{-3}). This approach was similarly used to derive deposition fluxes from an air quality

227   model, Global Environmental Multiscale – Modelling Air-quality and Chemistry (GEM-MaCH)

228   (Moran et al., 2010; also see SI Section S5 for details). The geographic surface area uncertainty

229   is estimated at 5%. Dry deposition fluxes between the sources and the first screen were also

230   estimated using ΔT based on the extrapolated transfer rates back to the source region ('extended'

231   region). The surface area boundaries for these 'extended' regions were determined using latitude

232   and longitude coordinates that were weighted by emissions. This was done by first using the

233   average wind direction from Screen 1 and creating a set of parallel back trajectories (~20)

234   starting at different parts of Screen 1 back across the source region. For **TON**, the NO_x emission

235   sources along each back trajectory were weighted by their NO_x emissions to obtain an emissions-

236   weighted center location with latitude and longitude coordinates for each back trajectory. The

237   line connecting these emissions-weighted center locations formed the boundary of the extended

238   surface area. The extended surface area was similarly determined for **TOS** based upon the

239   known locations of the major SO_2 point sources. The uncertainty of the 'extended' regions is

240   estimated at 10% based on repeated optimizations of the geographical area. Surface areas are

241   visualized as grey shaded regions between screens in Figure 1 and tabulated in SI Table S1.

242   Spatially-averaged dry deposition velocities, V_d, based on the aircraft measurements were

243   determined over the surface area between screens using average plume concentrations across

244   pairs of screens at about 40 meters above the ground for **TOS** and **TON** (e.g. Equation 6 for

245   SO_2).

246    $$V_d = \frac{F_{SO2}}{[SO2]} \qquad\qquad (6)$$

247   The largest source of uncertainty in V_d calculated this way was the determination of

248   concentration at 40 meters above the surface as the measurements were extrapolated from the

249   lowest aircraft altitude to the surface and interpolated concentrations were used. The

250   measurement-derived V_d are compared with those from GEM-MACH which uses inferential

251   methods.

252

253

254

255 **2.5 Monte-Carlo simulations of dry deposition velocities using multiple resistance-based**

256 **parameterizations**

257   Parameterization of dry deposition in inferential algorithms is commonly based on a

258 resistance approach with dry deposition velocity depending on three main resistance terms as

259 below:

260
$$V_d = \frac{1}{R_a + R_b + R_c}$$
(7)

261

262 where R_a, R_b and R_c represent the aerodynamic, quasi-laminar sublayer and bulk surface

263 resistances respectively. Although these resistance terms are common among many regional air

264 quality models (Wu et al., 2018), the formulae used (and inputs in to these formulae) to calculate

265 the individual resistance terms differ significantly among the inferential deposition algorithms.

266 To assess the potential for a general underestimation of V_d across different inferential deposition

267 algorithms, and to compare with the aircraft-derived V_d, five different inferential deposition

268 algorithms, including that used in the GEM-MACH model for calculating V_d (Wu et al., 2018)

269 were incorporated into a Monte-Carlo simulation for V_d for SO_2. NO_y was not considered here,

270 as its measurement includes multiple reactive nitrogen oxide species with different individual

271 deposition velocities. We note that many of the inferential algorithms are based on observations

272 of SO_2 and O_3 deposition made at single sites, and the extent to which a chemical is similar to

273 SO_2 or O_3 features into its V_d calculation – the comparison thus has relevance for species aside

274 from SO_2.

275   The five deposition algorithms considered are denoted ZHANG, NOAH-GEM, C5DRY,

276 WESLEY and GEM-MACH. To perform the simulations, formulae for the first four algorithms

277   were taken from Wu et al. (2018) and for GEM-MACH taken from Makar et al. (2018). The

278   stomatal resistance in the ZHANG algorithm was from Zhang et al. (2002). The GEM-MACH

279   formula (Equation 8.7 in the SI of Makar et al. (2018)) for mesophyll resistance R_{mx} contained a

280   typo (missing the Leaf Area Index (LAI)) and was corrected for as follows:

281   $$R_{mx} = [LAI(H^*/3000 + 100\,f_0)]^{-1} \tag{8}$$

282   Prescribed input values were constrained by the range of possible values consistent with the

283   conditions during the aircraft flights and are shown in SI Table S3 with associated references.

284   Calculations for the R_a term were based on unstable and dry conditions as observed during the

285   aircraft flights. The Monte-Carlo simulation generated a distribution of possible V_d values,

286   based on randomly generated values of the input variables to each algorithm and selected from

287   Gaussian distributions with a range of 3 sigma for all input parameters. All simulations were

288   performed with the same input values that were common between the algorithms.

289   **3 Results and Discussion**

290   **3.1 Meteorological and Emissions Conditions during the Transformation Flights**

291   During the experiments, the dry deposition rates (D) were quantified under different

292   meteorological conditions and emissions levels of **TOS** and **TON** (E_{TOS} and E_{TON}) for the three

293   flights (see Table 1). These differences played important roles in the observed pollutant

294   concentrations and resulting dry deposition fluxes for F7, F19 and F20. Mixed layer heights

295   (MLH) were derived from aircraft vertical profiles that were conducted in the centre of the

296   plume at each downwind set of transects. The profiles of temperature, dew point temperature,

297   relative humidity and pollutant mixing ratios were inspected for vertical gradients indicating a

298   contiguous layer connected to the surface. The highest MLH was determined for F7 at 2500

299   magl whereas F19 had the lowest MLH at 1200 magl (Table 1). In F20, the MLH was 2100

300   magl. The combination of a high MLH in F7 with the highest wind speeds resulted in the lowest

301   pollutant concentrations of the three flights. In F19, lower wind speeds and the lowest mixed

302   layer heights led to the highest pollutant levels. F20 had emissions and meteorological

303   conditions that were in between F7 and F19 resulting in pollutant concentrations between those

304   of F7 and F19.

305   Emission rates of SO_2 and NO_x (designated as E_{TOS} and E_{TON}) from the main sources in

306   the AOSR were estimated from the aircraft measurements and varied significantly between the

307   three flight days. The measurement-based emission rates of E_{TOS} and E_{TON} were taken from the

308   mass transfer rates of T_{SO2} and T_{NOy} (described in Methods) by extrapolating backwards to the

309   source locations in the AOSR using exponential functions (Figure 2, Section 3.2). For **TOS**, the

310   source location was set at 57.017N, -111.466W, where the main stacks for SO_2 emissions are

311   located. For **TON**, the source locations were determined from geographically weighted

312   locations. Emission rates E_{TOS} and E_{TON} for each flight are shown in Table 1.

313   Model-based E_{TOS} and E_{TON} were also obtained from the 2.5 km x 2.5 km gridded

314   emissions fields that were specifically developed for model simulations of the large AOSR

315   surface mining facilities (Zhang et al., 2018) i.e. Suncor Millenium, Syncrude Mildred Lake,

316   Syncrude Aurora North, Shell Canada Muskeg River Mine & Muskeg River Mine Expansion,

317   CNRL Horizon Project and Imperial Kearl Mine. The emissions fields have been used in GEM-

318   MACH (described in SI Section S5) to carry out a number of model simulations (Zhang et al.,

319   2018; Makar et al., 2018) including for the present study. In this work, emissions were summed

320   from various sources including offroad, point (Continuous Emissions Monitoring (CEMS)), and

321   point (non-CEMS) for the surface mines to obtain total AOSR hourly emission rates for the

322   flight time periods of interest (Table 2). The standard deviations reflect the emissions variations

323   during the simulated flight.

324   **3.2 Mass Transfer Rates**

325   The mass transfer rates T across the virtual flight screens for all three flights are shown

326   for **TOS** and **TON** in Figure 1 and plotted in Figure 2. In F20, two distinct **TON** plumes were

327   observed, allowing separate T calculations for **TON**. Monotonic decreases in T were observed

328   for both **TOS** and **TON** during transport downwind in all flights, clearly showing dry

329   depositional losses. The deposition rate D (Methods, Section 2.3) was used to estimate the

330   cumulative deposition of **TOS** and **TON** as a fraction of E_{TOS} or E_{TON} and is shown in Figure 3

331   for F7, F19 and F20 for transport distances of up to107-135 km downwind of the sources.

332   Curves were fitted to the **TOS** and **TON** dry deposition cumulative percentages from which $d_{1/e}$

333   and τ were determined (SI Table S1). The transport e-folding distance ($d_{1/e}$) was determined

334   where 63.2% of E_{TOS} (or E_{TON}) was dry deposited, i.e., $\sum_{d=0}^{d_{1/e}} D(d) = 0.368E_{TOS}$. The

335   atmospheric lifetimes (τ) were derived as $\tau = d_{1/e}/u$, where u was the average wind speed across

336   the distance $d_{1/e}$. These estimates were compared with predictions from the regional air quality

337   model GEM-MACH (Makar et al., 2018; Moran et al., 2010; SI Section S5) using facility

338   emission rates (Table 2). For **TOS** during F19, (Figure 3b, e), the observed cumulative

339   deposition at the maximum distance accounted for 74±5% vs. the modelled 21% of E_{TOS}, due

340   mostly to SO_2 dry deposition (>92%). Fitting a curve to D and interpolating the cumulative

341   deposition fraction to the 63.2% E_{TOS} loss leads to a $d_{1/e}$ of 71±1 km, versus 500 km for the

342   model prediction. Under the prevailing wind conditions, the observed distance indicates a τ for

343   **TOS** of approximately 2.2 hours, whereas the model prediction indicated 16 hours. Large

344   observation-based values and model prediction differences in lifetime were also evident for the

345   other flights (SI Table S1). Clearly, the model predictions significantly underestimated

346   deposition and vastly overestimated $d_{1/e}$ and τ. The observation-based values for τ are also lower

347   than average lifetimes of 1–2 days for SO_2 and 2–9 days for pSO_4 derived from global models

348   (Chin et al., 2000; Benkovitz et al., 2004; Berglen et al., 2004), which include the effects of wet

349   deposition and chemical conversion for SO_2, thus making their implicit residence times with

350   respect to dry deposition even longer.

351   For **TON** in F19 (Figure 3h, l), the observed cumulative deposition accounted for

352   49±11% of E_{TON} at the maximum flight distance, versus 19% predicted by the model. Similar

353   model underestimates for cumulative deposition fractions were found for F7 and F20.

354   Extrapolating to the 63.2% cumulative deposition fraction, $d_{1/e}$ was estimated to be 190±7 km for

355   F19 versus a predicted 650 km from the model, implying a τ of approximately 5.6 hours for the

356   measurement-based results and 23 hours for the model prediction. Again, analogous differences

357   for F7 and F20 were found (SI Table S1). Similar to TOS, the measurement-based $d_{1/e}$ and τ

358   values for TON were significantly smaller than commonly accepted lifetimes of a few days for

359   nitrogen oxides in the boundary layer (Munger et al., 1998).

360   **3.3 Dry Deposition Fluxes F**

361   Using D, the average dry deposition fluxes, F (in tonnes S or N km^2 hr^{-1}), were calculated

362   by dividing D by the plume footprint surface areas estimated by extending to the plume edges

363   where the concentrations fell to background levels (Methods, Section 2.4). These footprints are

364   shown as the gray shaded geographic areas in Figure 1, totaling 3500, 5700 and 4200km^2 for F7,

365   F19, and F20 plumes, respectively; see SI Table S1 for **TON** plume areas). Figure 4a shows

366   F_{TOS} values for all three flights, exhibiting exponential decreases with increasing distance away

367   from the sources and showing e-folding distances for F_{TOS} of 18, 27, and 55 km for F7, F19, and

368   F20, respectively. More than 90% of the decreases in F_{TOS} were accounted for by F_{SO2}.

369   Similarly, F_{TON} decreased exponentially with increasing transport distances in all flights (Figure

370   4c), exhibiting e-folding distances of 18 and 33 km for F7 and F19, and 55 and 189 km for the

371   south and north **TON** plumes during F20, respectively. These e-folding distances were similar to

372   those for F_{TOS}, indicating similar rates of decreases in F_{TON} with transport distances.

373   As expected from the τ and transport e-folding distance $d_{1/e}$ comparisons, the GEM-

374   MACH model F_{TOS} were significantly lower than the measurement-based F_{TOS} results (Figure

375   4a), with the model F_{TOS} e-folding distances usually large: 133, 797, and 57 km for F7, F19, and

376   F20, respectively, or 7.4, 29.5, and 1.1 times longer than the corresponding measurement results.

377   Part of the differences between model and measurement F_{TOS} could be explained by differences

378   in actual versus model emissions, E_{TOS} (Tables 1 vs 2). To remove the influence of emissions,

379   an emission-normalized flux ($=F_{TOS}/E_{TOS}$ and F_{TON}/E_{TON}) was calculated for both measurement

380   and model (SI Figure S1). Figure 4b shows the ratios of measurement to model normalized

381   emissions for TOS. The model emission-normalized fluxes F_{TOS}/E_{TOS} were lower than the

382   measurement-based values by factors of 2.5-14, 1.8-3.4, and 2.0-3.0 for F7, F19, and F20,

383   respectively, decreasing with increased transport distances. However, they coalesce to a factor

384   of 2 at the furthest distances sampled by the aircraft, indicating that the model F_{TOS} estimates

385   were biased low by similar factors. The decreasing trends suggest that at distances further

386   downwind, model fluxes may exceed measurement-based fluxes, albeit at magnitudes lower than

387   those shown in Figure 4a, which is consistent with earlier study results (Makar et al., 2018). For

388   F_{TON}, the model-predicted values were also lower than the measurement results, especially near

389   the sources (Figure 4c), and showed little variation with transport distances for all flights, in

390   strong contrast to the exponential decays observed from the aircraft. However, the emission-

391   normalized fluxes (=F_{TON}/E_{TON}) for the model approached those from measurements within

392   maximum flying distances for F19 and F20, although still significantly lower for F7 (>10x)

393   (Figure 4d).

394   **3.4 Dry Deposition Velocities V_d**

395   The shorter $d_{1/e}$ and τ, and larger deposition fluxes F near the sources determined from

396   the aircraft measurements compared to predictions by the GEM-MACH model indicate that the

397   model V_d was underestimated. Gas-phase V_d in the model is predicted with a standard inferential

398   "resistance" algorithm (Wesley, 1989; Jarvis, 1976), with resistance to deposition calculated for

399   multiple parameters including aerodynamic, quasi-laminar sublayer and bulk surface resistances

400   (Baldocchi, 1987). To demonstrate the model underestimation in V_d, comparisons between the

401   measurement-based and model V_d were made where an evaluation of V_d for **TOS** and **TON** was

402   possible. All F_{SO2} were converted into $V_{d\text{-}SO2}$ by dividing F_{SO2} by interpolated SO_2

403   concentrations at 40 meters above ground, averaging 1.2±0.5, 2.4±0.4, and 3.4±0.6 cm s^{-1} for F7,

404   F19 and F20, respectively, across the plume footprints (Methods, Section 2.4 and SI Table S2).

405   The corresponding model $V_{d\text{-}SO2}$ derived in the same way as the observations was 0.72, 0.63, and

406   0.58 cm s^{-1}, 1.7-5.4 times lower than observations (SI Section S5; SI Table S2). Interestingly,

407   the median V_d for SO_2 of 4.1 cm s^{-1} determined using eddy covariance/vertical gradient

408   measurements from a tower in the AOSR is higher than the mass balanced method showing an

409   even larger discrepancy compared to the model (SI Section S3; Figure S4). Similarly, derived

410    $V_{d\text{-}TON}$ averaged 2.8±0.8, 1.6±0.5, 4.7±1.4 and 2.2±0.7 cm s^{-1} F7, F19, F20 south plume, and F20

411   north plume, respectively (SI Table S2), 1.2-5.2 times higher than the corresponding modelled

412    $V_{d\text{-}TON}$ of 1.4, 1.3, 0.92, and 0.90 cm s^{-1}.

413

3.5 Monte-Carlo simulations of V_d for SO$_2$

414

415   To further demonstrate observation-model differences, V_d distributions of SO$_2$ from five

416   common inferential dry deposition algorithms (Wu et al., 2018; Makar et al., 2018) were

417   determined for the conditions encountered during the flights using a Monte-Carlo approach as

418   described in Methods, Section 2.5). Results for the V_d simulations algorithms are shown in

419   Figure 5a. Histograms for all five algorithms have peak V_d values at ~1 cm s^{-1} or lower.

420   Probability distributions for the individual resistance terms, R_a, R_b, and R_c showed that the

421   dominant resistance driving V_d was the R_c term (SI Figure S2). Also shown in Figure 5a are the

422   measurement-derived V_d for Flights 7, 19 and 20, and that from the Oski-ôtin ground site. The

423   observed V_d values are larger than the V_d values for most of the simulations, with the exception

424   of Flight 7, where the Zhang et al. (2002), NOAH-GEM (Wu et al., 2018) and C5DRY (Wu et

425   al., 2018) algorithms' distributions agree with the observations. All algorithms are biased low

426   relative to the observations for the remaining flights, and the Oski-ôtin ground site.   It is noted

427   that the ground-site observations that were derived using a standard flux tower methodology (SI

428   Section S3) at a single site, appeared to be higher than all other V_d; nevertheless, these

429   observations are closer to the aircraft values than the algorithm estimates. These results indicate

430   that an underestimation of V_d relative to both aircraft and ground based measurements in the

431   AOSR region is not unique to the GEM-MACH model or its dry deposition algorithm; similar

432   results would occur with the other algorithms included in the Monte-Carlo simulations, all of

433   which are used within other regional models.

434   To investigate the possible reasons behind the low model V_d relative to the observations,

435   a series of sensitivity tests using SO$_2$ were conducted. Differences in model V_d have been shown

436   to be mainly due to differences in the calculated R_c (Wu et al., 2018), and sensitivity tests here

437   indicated that R_c is particularly sensitive to the cuticular resistance R_{cut}. Hence, factors causing

438   R_{cut} to change can have significant impact on model V_d. In some of the algorithms, R_{cut} and

439   other resistance terms are dependent on the effective Henry's Law constant K_H^* for SO_2. The

440   Monte-Carlo simulations for Figure 5 assumed a surface pH= 6.68 resulting in a K_H^* of 1×10^5 for

441   SO_2. Additional Monte-Carlo simulations were performed for the GEM-MACH dry deposition

442   algorithm by adjusting K_H^* assuming different pH with small variations from a pH=6.68

443   significantly changing R_c, R_{cut}, and V_d (SI Figure S3). In Figure 5b – red dashed line, with a

444   surface pH change from 6.68 to 8, consistent with possible alkaline surfaces in the AOSR

445   (Makar et al., 2018), in the GEM-MACH simulation, the V_d distribution is moved to larger

446   values) with its peak value shifting from 0.6 to 1.4 cm s^{-1}. These results show that model V_d may

447   be highly sensitive to assumed surface pH, at least when using some inferential dry deposition

448   algorithms which are pH-dependent. However, Figure 5b shows that this pH-associated increase

449   in V_d is still insufficient to encompass the range of measurement-derived V_d. Increasing pH to 8

450   for the GEM-MACH simulation reduces R_{cut}, hence R_c, to values much smaller than R_a and R_b,

451   suggesting that model V_d cannot further increase without reductions in both R_a and R_b. In other

452   words, R_a and R_b were probably overestimated in the current deposition velocity algorithms. By

453   using the Zhang et al. (2002) R_a and the NOAH-GEM (Wu et al., 2018) R_b parameterizations in

454   the GEM-MACH algorithm, a further shift of the GEM-MACH V_d distribution to larger values

455   was found, with the range encompassing most of the observations (Figure 5b, pink dashed line).

456   Clearly, from the Monte-Carlo simulations for SO_2 V_d comparisons, inferential dry

457   deposition algorithms as used in regional and global chemical transport models need to be further

458   validated and improved, especially over large geographic regions. Here, the role of pH was

459   identified for improvement in some algorithms along with possible improvement in aerodynamic

460   and quasi-laminar sublayer resistance parameters. Yet, for other algorithms and for **TON**

461   compounds, the model low-biases in V_d remain to be investigated.

462   The underestimates suggest that the applications of these algorithms in regional or global

463   models may significantly underestimate model predictions of **TOS** dry depositional loss from the

464   atmosphere. Underestimates in V_d are the result of a combination of uncertainties in the

465   parameterizations of each algorithm. In the case of the algorithm used in GEM-MACH, by

466   adjusting the assumed surface pH from 6.68 to 8 (justifiable given the considerable dust

467   emissions in the region (Zhang et al., 2018)), the model V_d moved closer to the aircraft-derived

468   values (Figure 5b), reducing the model-observation gap by approximately 2/3. In addition,

469   substituting the aerodynamic resistance and quasi-laminar sublayer resistance parameterizations

470   in the GEM-MACH algorithm with that from Zhang et al. (2002) and NOAH-GEM (Wu et al.,

471   2018), respectively, resulted in a further increase in the model V_d distribution that encompasses

472   most of the observations (Figure 5b). Clearly, different algorithms respond differently to

473   changes in the parameterizations, and validation and adjustment to each algorithm needs

474   measurement-based results over large regions such as derived here.

475

476   **4 Conclusions**

477   The atmospheric transport distances and lifetimes $d_{1/e}$ and τ determined from the aircraft

478   measurements are substantially shorter than the GEM-MACH model predictions, and the dry

479   deposition fluxes and velocities F and V_d near sources are larger compared to the predictions by

480   GEM-MACH and five inferential dry deposition velocity algorithms, respectively. There are

481   important implications for these measurement-model discrepancies. Such discrepancies indicate

482   that regional or global chemical transport models using these algorithms are biased low for local

483   deposition and high for long-range transport and deposition, and **TOS** and **TON** loss from the

484   atmosphere are significantly under-predicted, resulting in overestimated lifetimes. Moreover,

485   emissions assessed through network measurements or budget analysis of atmospheric **TOS** and

486   **TON** (Sickles and Shadwick, 2015; Paulot et al., 2018; Berglen et al., 2004) may be

487   underestimated due to lower V_d used in these estimates, and may require reassessing the

488   effectiveness of control policies. Shorter τ for **TOS** and **TON** reduces their atmospheric spatial

489   scale and intensity of smog episodes, potentially reducing human exposures (Moran et al., 2010).

490   Importantly, shorter τ for **TOS** and **TON** reduces their contribution to atmospheric aerosols;

491   consequently, the negative direct and indirect radiative forcing from these sulfur and nitrogen

492   aerosols are reduced, reducing their cooling effects on climate (Solomon et al., 2007). These

493   impacts suggest that more measurements to determine τ and F for these pollutants across large

494   geographic scales and different surface types are necessary to better quantify their climate and

495   environmental impacts in support of policy. While in the past such determination was difficult

496   and/or impossible, the present study provides a viable methodology to achieve such a goal.

497

498

499   **Table 1.** Average observed meteorological conditions and facility emission rates of **TOS** (E_{TOS})
500   and **TON** (E_{TON}), (determined from extrapolated (to distance=0) transfer rates; Figure 1) for
501   **TOS** and **TON** during the F7, F19 and F20 flights. SP=south plume; NP=north plume.

Flight	Date	Time (UTC)	Mean wind speed (m/s)	Mean wind direction (°)	Mixed layer height (m agl)	E_{TOS} (t/hr)	E_{TON} (t/hr)
7	Aug 19/13	2007–0108	13.0±1.0	256±11.7	2500±100	3.4	1.2
19	Sep 4/13	1854–2353	9.5±1.9	218±16	1200±100	18.5	3.9
20	Sep 5/13	1933-2436	8.9±1.2	281±11	2100±100	5.8	2.2 (SP) 1.2 (NP)

502

503   **Table 2**. Model average meteorological conditions and facility emission rates of **TOS** (E_{TOS}) and
504   **TON** (E_{TON}) during the F7, F19 and F20 flights as described above. SP=south plume; NP=north
505   plume.

Flight	Date	Time (UTC)	mean wind speed (m/s)	mean wind direction (°)	mixed layer height (m agl)	E_{TOS} (t/hr)	E_{TON} (t/hr)
7	Aug 19/13	2007–0108	12.6±0.3	253±5.0	1670±80	3.8	2.9
19	Sep 4/13	1854–2353	8.1±1.0	225±4.6	1450±43	4.3	2.4
20	Sep 5/13	1933-2436	9.1±0.7	275±1.6	1590±42	3.7	1.5 (SP) 0.9 (NP)

506
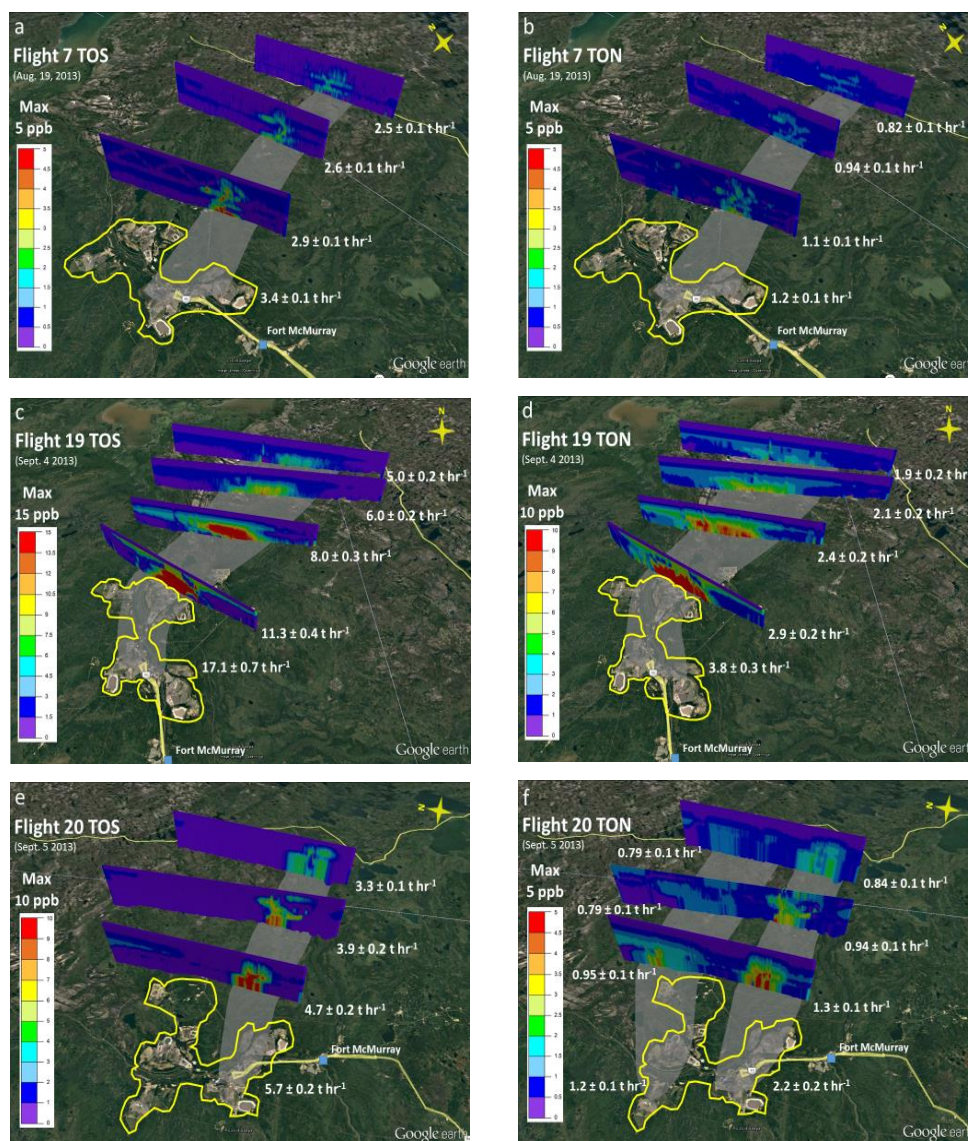
Figure 1. **TOS** and **TON** plumes downwind of the AOSR during three Lagrangian flights, F7, F19 and F20. The AOSR facilities are enclosed by the yellow outline. The transfer rates T in tonnes S or N hr^{-1} across each screen are shown. The grey shaded surface areas are identified as the geographic footprint under the plumes. Data: Google, Image 2016 Digital Globe © Google Maps.
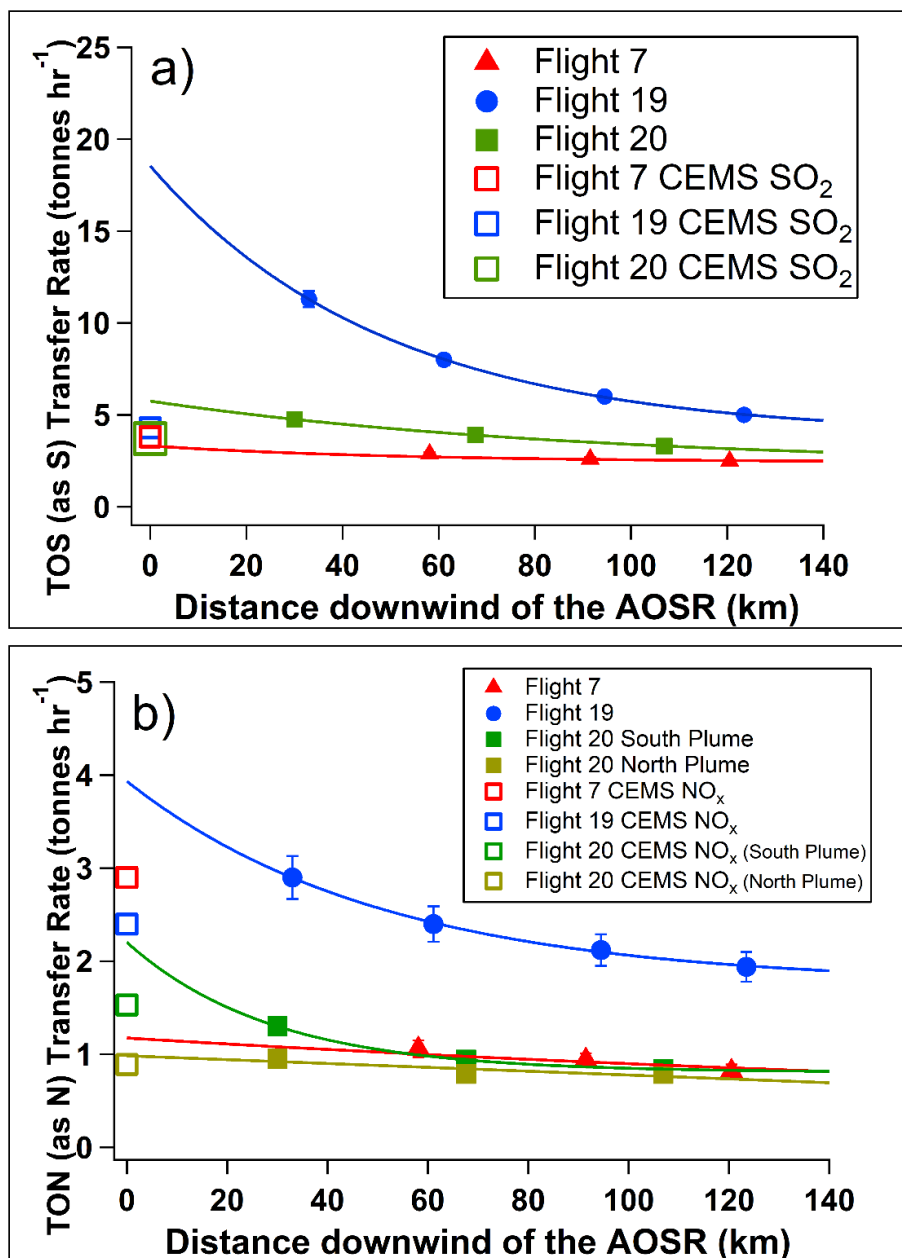
519

520 **Figure 2**. TERRA-derived transfer rates of (a) **TOS** and (b) **TON** for F7, F19 and F20. The
521 vertical bars indicate the propagated uncertainties. The model emission rates E_{TOS} and E_{TON} are
522 shown by the open symbols.

523
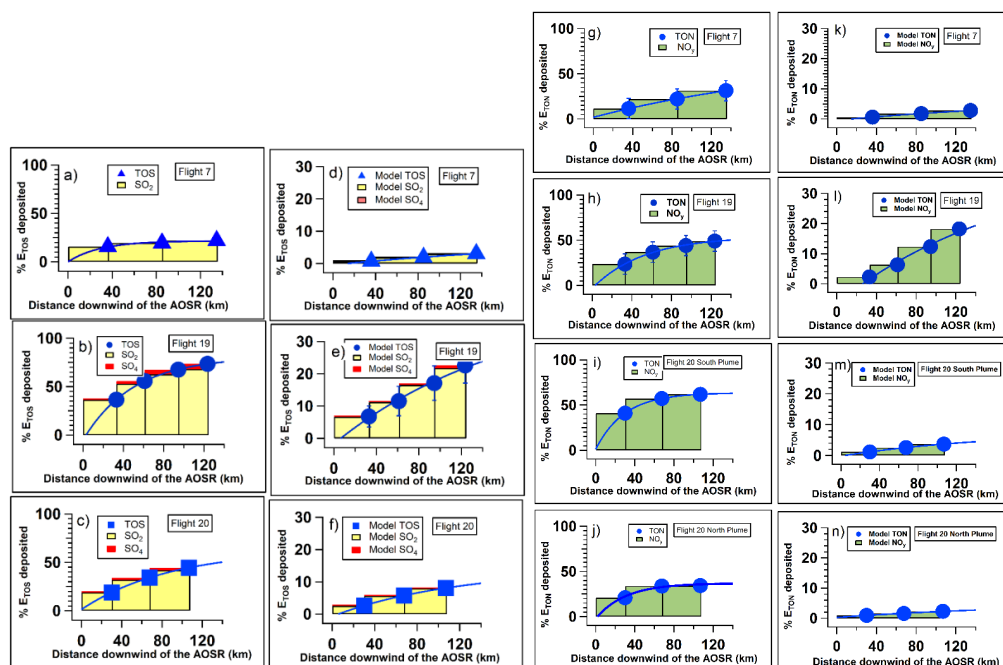
Figure 3. Cumulative dry deposition as a percentage of emissions of E_{TOS} E_{TON} for F7, F19 and F20 measurements and GEM-MACH model predictions. The bars show the dry deposition due to SO_2 and pSO_4. The curves were fitted to the **TOS** and **TON** dry deposition percentages from which $d_{1/e}$ and τ were determined.

528
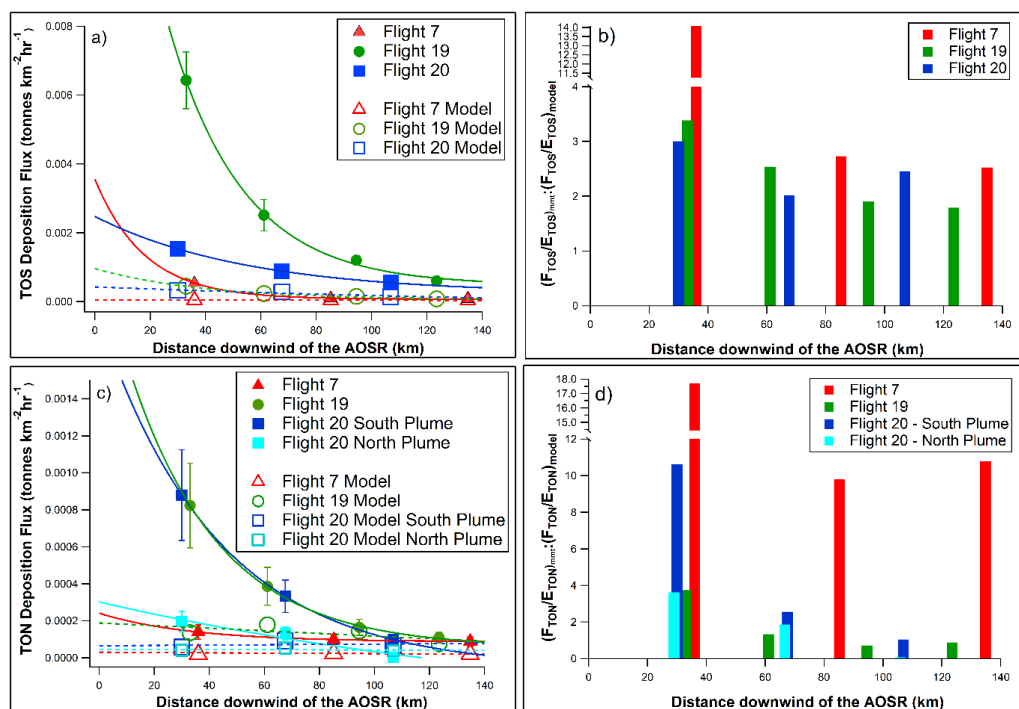
Figure 4. Dry deposition fluxes F_{TOS} and F_{TON} determined from measurements (solid symbols)
and GEM-MACH model predictions (open symbols). (a) F_{TOS}, (b) ratios of measurement to
model normalized emissions F_{TOS}/E_{TOS}, (c) F_{TON}, and (d) ratios of measurement to model
normalized emissions F_{TON}/E_{TON}.

534
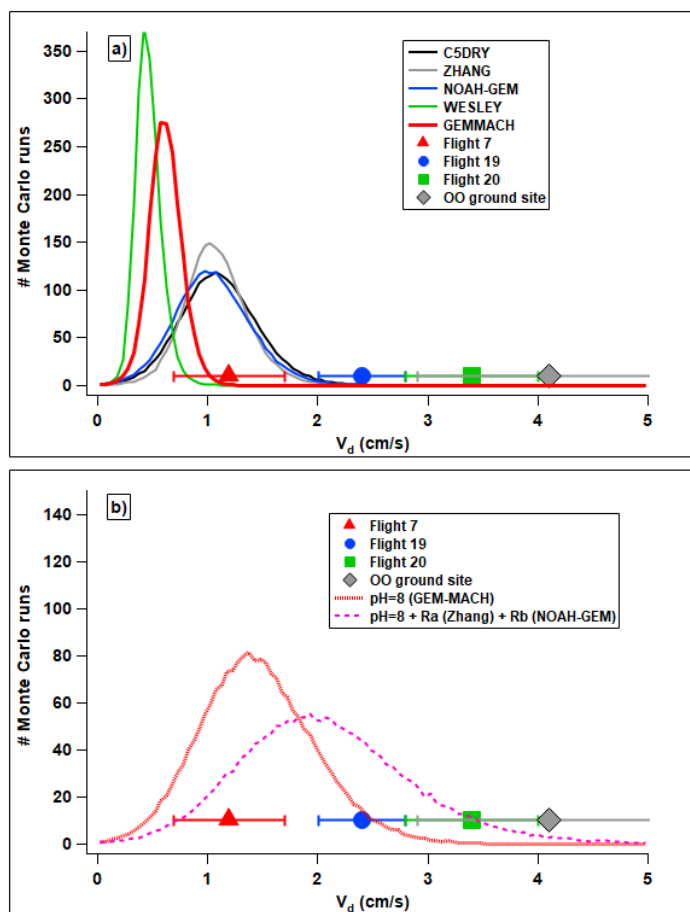
Figure 5. (a) Distributions of V_d for SO₂ from Monte-Carlo simulations using 5 different
deposition parameterizations (Wu et al., 2018; Makar et al., 2018) and (b) Monte-Carlo
simulations for the GEM-MACH algorithm using a pH=8 and using a pH=8 plus replacing the
GEM-MACH algorithm R_a and R_b formulae with that from Zhang et al. (2002) and NOAH-GEM
(Wu et al., 2018), respectively. Aircraft-derived V_d for F7, F19 and F20 as well as the median
value for the Oski-ôtin ground site (SI Figure S4) are shown in both (a) and (b) for comparison.

541

References

Aubinet, M., Vesala, T. and Papale, D. (Eds.): Eddy Covariance. Springer Atmospheric Sciences, Springer, Dordrecht, 2012.

Baldocchi, D.D., Vogel, C.A., and Hall, B.: A canopy stomatal resistance model for gaseous deposition to vegetated surfaces, Atmos. Env., **21**, 91-101, https://doi.org/10.1016/0004-6981(87)90274-5, 1987.

Baray, S., Darlington, A., Gordon, M., Hayden, K.L., Leithead, A., Li, S.-M., Liu, P.S.K., Mittermeier, R.L., Moussa, S.G., O'Brien, J., Staebler, R., Wolde, M., Worthy, D. and McLaren, R.: Quantification of methane sources in the Athabasca Oil Sands Region of Alberta by aircraft mass balance, Atmos. Chem. Phys., **18**, 7361-7378, https://doi.org/10.5194/acp-18-7361-20182018.

Benkovitz, C.M., Schwartz, S.E., Jensen, M.P., Miller, M.A., Easter, R.C. and Bates, T.S.: Modeling atmospheric sulfur over the Northern Hemisphere during the Aerosol Characterization Experiment 2 experimental period, J. Geophys. Res., **109**, D2220, https://doi.org/10.1029/2004JD004939, 7, 2004.

Berglen, T.F., Berntsen, T.K., Isaksen, I.S.A. and Sundet, J.K.: A global model of the coupled sulfur/oxidant chemistry in the troposphere: The sulfur cycle, J. Geophys. Res., **109**, D19310, https://doi.org/10.1029/2003JD003948, 2004.

Bobbink, R., Hicks, K., Galloway, J., Spranger, T., Alkemade, R., Ashmore, M., Bustamante, M., Cinderby, S., Davidson, E., Dentener, F., Emmett, B., Erisman, J-W., Fenn, M., Gilliam, F., Nordin, A., Pardo, L. and De Vries, W.: Global assessment of nitrogen deposition effects on terrestrial plant diversity: a synthesis, Ecol. Appl. **20**, 30-59, https://doi.org/10.1890/08-1140.1, 2010.

Brook, J.R., Di-Giovanni, F., Cakmak, S. and Meyers, T.P.: Estimation of dry deposition velocity using inferential models and site-specific meteorology – uncertainty due to siting of meteorological towers, Atmos. Environ., **31**, 3911-3919, https://doi.org/10.1016/S1352-2310(97)00247-1, 1997.

Chin, M., Savoie, D.L., Huebert, J., Bandy, A.R., Thornton, D.C., Bates, T.S., Quinn, P.K., Saltzman, E.S. and De Bruyn, W.J.: Atmospheric sulfur cycle simulated in the global model GOCART: Comparison with field observations and regional budgets, J. Geophys. Res., **105**, 24689-24712, https://doi.org/10.1029/2000JD900384, 2000.

Christian, G., Ammann, M., D'Anna, B., Donaldson, D.J. and Nizkorodov, S.A.: Heterogeneous photochemistry in the atmosphere, Chem. Rev. **115**, 4218-4258, https://doi.org/10.1021/cr500648z, 2015.

DeCarlo, P.F. , Kimmel, J.R., Trimborn, A., Northway, M.J., Jayne, J.T., Aiken, A.C., Gonin, M., Fuhrer, K., Horvath, T., Docherty, K.S., Worsnop, D.R., Jimenez, J.L.: Field-deployable, high-resolution, time-of-flight aerosol mass spectrometer, Anal. Chem., 8281-9289, https://doi.org/10.1021/ac061249n, 2006.

580 Degrazia, G.A., Maldaner, S., Buske, D., Rizza, U., Buligon, L., Cardoso, V., Roberti, D.R.,
581   Acevedo, O., Rolim, S.B.A. and Stefanello, M.B.: Eddy diffusivities for the convective
582   boundary layer derived from LES spectral data, Atmos. Pollut. Res., **6**, 605-611,
583   https://doi.org/10.5094/APR.2015.068, 2015.

584 Dentener, F., Drevet, J., Lamarque, J.F., Bey, I., Eickhout, B., Fiore, A.M., Hauglustaine, D.,
585   Horowitz, L.W., Krol, M., Kulshrestha, U.C., Lawrence, M., Galy-Lacaux, C., Rast, S.,
586   Shindell, D., Stevenson, D., Van Noije, T., Atherton, C., Bell, N., Bergman, D., Butler, T.,
587   Cofala, J., Collins, B., Doherty, R., Ellingsen, K., Galloway, J., Gauss, M., Montanaro, V.,
588   Müller, J.F., Pitari, G., Rodriguez, J., Sanderson, M., Solmon, F., Strahan, S., Schultz, M.,
589   Sudo, K., Szopa, S. and Wild, O.: Nitrogen and sulfur deposition on regional and global
590   scales: A multimodel evaluation, Global Biogeochem. Cycle, **20**, GB4003,
591   https://doi.org/10.1029/2005GB002672, 2006.

592 Doney, S.C. The growing human footprint on coastal and open-ocean biogeochemistry, Science
593   **328**, 1512-1516, DOI: 10.1126/science.1185198, 2010.

594 Finkelstein, P.L., Ellestad, T.G., Clarke, J.F., Meyers, T.P., Schwede, D.B., Hebert E.O. and
595   Neal, J.A.: Ozone and sulfur dioxide dry deposition to forests: Observations and model
596   evaluation, J. Geophys. Res., **105**, 15365-15377, https://doi.org/10.1029/2000JD900185,
597   2000.

598 Fowler, D., Pilegaard, K., Sutton, M.A., Ambus, P., Raivonen, M., Duyzer, J., Simpson, D.,
599   Fagerli, H., Fuzzi, S., Schjoerring, J.K., Granier, C., Neftel, A., Isaksen, I.S.A., Laj, P.,
600   Maione, M., Monks, P.S., Burkhardt, J., Daemmgen, U., Neirynck, J., Personne, E., Wichink-
601   Kruit, R., Butterbach-Bahl, K., Flechard, C., Tuovinen, J.P., Coyle, M., Gerosa, G., Loubet,
602   B., Altimir, N., Gruenhage, L., Ammann, C., Cieslik, S. Paoletti, E., Mikkelsen, T.N., Ro-
603   Poulsen, H., Cellier, P., Cape, J.N., Horváth, L., Loreto, F., Niinemets, Ü., Palmer, P.I.,
604   Rinne, J., Misztal, P., Nemitz, E., Nilsoon, D., Pryor, S., Gallagher, M.W., Vesala, T., Skiba,
605   U., Bruggemann, N. Zechmeister-Boltenstern, S., Williams, J., O'Dowd, Facchini, M.C., de
606   Leeuw, G., Flossman, A., Chaumerliac, N. and Erisman, J.W.: Atmospheric composition
607   change: ecosystems-atmosphere interactions, Atmos. Environ., **43**,
608   https://doi.org/10.1016/j.atmosenv.2009.07.068, 5193-5267, 2009.

609 Gordon, M., Li, S.-M., Stabler, R., Darlington, A., Hayden, K., O'Brien, J. and Wolde, M.:
610   Determining air pollutant emission rates based on mass balance using airborne measurement
611   data over the Alberta oil sands operations, Atmos. Meas. Tech., **8**, 3745-3765,
612   https://doi.org/10.5194/amt-8-3745-2015, 2015.

613 Howarth, R.W. Review: coastal nitrogen pollution: a review of sources and trends globally and
614   regionally, Harmful Algae, **8**, 14-20, https://doi.org/10.1016/j.hal.2008.08.015, 2008.

615 Jarvis, P.G. The interpretation of the variations in leaf water potential and stomatal conductance
616   found in canopies in the field, Phil. Trans. R. Soc. Lond., B., **273**, 593-610,
617   https://doi.org/10.1098/rstb.1976.0035, 1976.

618 Li, S.-M., Leithead, A., Moussa, S.G., Liggio, J., Moran, M.D., Wang, D., Hayden, K.,
619   Darlington, A., Gordon, M., Staebler, R., Makar, P.A., Stroud, C.A., McLaren, R., Liu,

P.S.K., O'Brien, J., Mittermeier, R.L., Zhang, J., Marson, G., Cober, S.G., Wolde, M. and Wentzell, J.J.B.: Differences between measured and reported volatile organic compound emissions from oil sands facilities in Alberta, Canada, Proc. Natl. Acad. Sci., **114**, E3756-E3765, https://doi.org/10.1073/pnas.1617862114, 2017.

Liggio, J., Li, S.-M., Hayden, K., Taha, Y.M., Stroud, C., Darlington, A., Drollette, B.D., Gordon, M. Lee, P., Liu, P., Leithead, A., Moussa, S.G., Wang, D., O'Brien, J., Mittermeier, R.L., Brook, J.R., Lu, G., Staebler, R., Han, Yuemei, Tokarek, T.W., Osthoff, H.D., Makar, P.A., Zhang, J., Plata, D.L. and Gentner, D.R.: Oil sands operations as a large source of secondary organic aerosols, Nature, **534**, 91-94, https://doi.org/10.1038/nature17646, 2016.

Liggio, J., Li, S.-M., Staebler, R., Hayden, K., Darlington, A., Mittermeier, R.L., O'Brien, J., McLaren, R., Wolde, M. Worthy, D. and Vogel, F.: Measured Canadian oil sands CO2 emissions are higher than estimates made using internationally recommended methods, Nature Comm., **10**, 1863, https://doi.org/10.1038/s41467-019-09714-9, 2019.

Makar, P.A., Akingunola, A., Aherne, J., Cole, A.S., Aklilu, Y., Zhang, J., Wong, I., Hayden, K., Li, S.-M., Kirk, J., Scott, K., Moran, M.D., Robichaud, A., Cathcart, H., Baratzedah, P., Pabla, B., Cheung, P., Zheng, Q. and Jeffries, D.S.: Estimates of exceedances of critical loads for acidifying deposition in Alberta and Saskatchewan, Atmos. Chem. Phys., **18**, 9897-9927, https://doi.org/10.5194/acp-18-9897-2018, 2018.

Matsuda, K., Watanabe, I., Wingpud, V. and Theramongkol, P.: Deposition velocity of O_3 and SO_2 in the dry and wet season above a tropical forest in northern Thailand, Atmos. Environ., **40**, 7557-7564, https://doi.org/10.1016/j.atmosenv.2006.07.003, 2006.

Meyers, T.P., Hicks, B.B., Hosker Jr, R.P., Womack, J.D. and Satterfield, L.C.: Dry deposition inferential measurement techniques. II. Seasonal and annual deposition rates of sulfur and nitrate, Atmos. Environ., **25**, 2631-2370, https://doi.org/10.1016/0960-1686(91)90110-S, 1991.

Moran, M.D., Ménard, S., Pavlovic, R., Anselmo, D., Antonopoulos, S., Makar, P.A., Gong, W., Gravel, S., Stroud, C., Zhang, J., Zheng, Q., Robichaud, A., Landry, H., Beaulieu, P.-A., Gilbert, S., Chen, J. and Kallaur, A.: Recent advances in Canada's national operational AQ forecasting system. In: Steyn DG, Rao ST (Eds) Air Pollution Modelling and Its Application, Springer, Dordrecht, 289, https://www.researchgate.net/deref/http%3A%2F%2Fdx.doi.org%2F10.1007%2F978-94-007-5577-2_37, 2010.

Munger, J.W., Fan, S., Bakwin, P.S., Goulden, M.L., Goldstein, A.H., Colman, A.S. and Wolfsy, S.C.: Regional budgets for nitrogen oxides from continental sources: Variations of rates for oxidation and deposition with season and distance from source regions, J. Geophys. Res., **103**, 8355-8368, https://doi.org/10.1029/98JD00168, 1998.

Paulot, F., Malyshev, S., Nguyen, T., Crounse, J.D., Shevliakova, E. and Horowitz, L.W.: Representing sub-grid scale variations in nitrogen deposition associated with land use in a global Earth system model: implications for present and future nitrogen deposition fluxes over

659   North America, Atmos. Chem. Phys. **18**, 17963-17978, https://doi.org/10.5194/acp-18-17963-
660   2018, 2018.

661 Samset, B.H., Myhre, G., Herber, A., Kondo, Y., Li, S.-M., Moteki, N., Koike, M., Oshima, N.,
662   Schwarz, J.P., Balkanski, Y., Bauer, S.E., Bellouin, N., Berntsen, T.K., Bian, H., Chin, M.,
663   Diehl, T., Easter, R.C., Ghan, S.J., Iversen, T., Kirkevåg, A., Lamarque, J.-F., Lin, G., Liu,
664   X., Penner, J.E., Schulz, M., Seland, Ø., Skeie, R.B., Stier, P., Takemura, T., Tsigaridis, K.
665   and Zhang, K.: Modelled black carbon radiative forcing and atmospheric lifetime in AeroCom
666   Phase II constrained by aircraft observations, Atmos. Chem. Phys. **14**, 12465–12477,
667   doi:10.5194/acp-14-12465-2014, 2014.

668 Sickles, J.E. & Shadwick, D.S. Air quality and atmospheric deposition in the eastern US: 20
669   years of change. Atmos. Chem. Phys., **15**, 173-197, https://doi.org/10.5194/acp-15-173-2015,
670   2015.
671
672 Solomon, S., Quin, M., Manning, Z., Chen, M. Marquis, K.B., Averyt, M., Tignor, M., and
673   Miller, H.L. (Eds): Climate Change 2007: The Physical Science Basis, IPCC *AR4*,
674   Cambridge University Press, 2007.

675 Stull, R. Introduction to Boundary Layer Meteorology, Kluwer Academic Press, 1988.

676 Vet, R., Artz, R.S., Carou, S., Shaw, M., Ro, C.-U., Aas, W., Baker, A., Bowersox, V.C.,
677   Dentener, F., Galy-Lacaux, C., Hou, A., Pienaar, J., Gillett, R., Forti, M.C., Gromov, S., Hara,
678   H., Khodzher, T., Mahowald, N.M., Nickovic, S., Rao, P.S.P. and Reid, N.W.: A global
679   assessment of precipitation chemistry and deposition of sulfur, nitrogen, sea salt, base cations,
680   organic acids, acidity and pH, and phosphorus, Atmos. Environ., **93**, 3-100,
681   https://doi.org/10.1016/j.atmosenv.2013.10.060, 2014.

682 Wesley, M.L. Parameterization of surface resistances to gaseous dry deposition in regional-scale
683   numerical models, Atmos. Environ.*, **23**, 1293-1304,
684   https://ui.adsabs.harvard.edu/link_gateway/1989AtmEn..23.1293W/doi:10.1016/0004-
685   6981(89)90153-4, 1989.

686 Wesley, M.L. & Hicks, B.B. A review of the current status of knowledge on dry deposition,
687   Atmos. Environ.*, **34,** 2261-2282,
688   https://ui.adsabs.harvard.edu/link_gateway/2000AtmEn..34.2261W/doi:10.1016/S1352-
689   2310(99)00467-7, 2000.

690 WHO, Ambient Air Pollution: A Global Assessment of Exposure and Burden of Disease, 2016.

691 Wright, L.P., Zhang, L., Cheng, I. and Aherne, J.: Impacts and effects indicators of atmospheric
692   deposition of major pollutants to various ecosystems - a review, Aerosol Air Quality Res., **18**,
693   1953-1992, https://doi.org/10.4209/aaqr.2018.03.0107, 2018.

694 Wu, Z., Schwede, D.B., Vet, R., Walker, J.T. Shaw, M. Staebler, R. and Zhang, L.: Evaluation
695   and intercomparison of five North American dry deposition algorithms at a mixed forest site,
696   J. Adv. Mod. Earth Sys., **10**, 1571-1586, https://doi.org/10.10292017MS001231, 2018.

Zhang, L., Moran, M.D., Makar, P., and Brook, J.R.: Modelling gaseous dry deposition in AURAMS: a unified regional air-quality modelling system, Atmos. Environ., **36**, 537-560, 2002.Zhang, J., Moran, M.D., Zheng, Q., Makar, P.A., Baratzadeh, P., Marson, G., Liu, P. and Li, S.-M.: Emissions preparation and analysis for multiscale air quality modeling over the Athabasca Oil Sands Region of Alberta, Canada, Atmos. Chem. Phys., **18**, 10459-10481, https://doi.org/10.5194/acp-18-10459-2018, 2018.

Author Contribution:

KH, SML, JL, SM, RM, RS, JO, MW all contributed to the collection of aircraft observations in the field. KH, RM and JO made the SO_2, NO_y and pSO_4 measurements and carried out subsequent QA/QC of data. RM analyzed canister VOCs and provided OH concentration estimates. SM provided OH estimates from MCM modelling as a comparison. AD contributed to the development of TERRA. JL wrote the Monte Carlo code. PM and AA ran the model and provided model analyses. JZ provided emissions data. LZ and RS provided deposition algorithm parameters. KH and SML wrote the paper input from all co-authors.

Code availability

All the computer code associated with the TERRA algorithm, including for the kriging of pollutant data, a demonstration dataset and associated documentation is freely available upon request. The authors request that future publications which make use of the TERRA algorithm cite this paper, Gordon et al., Liggio et al., or Li et al. as appropriate.

Data availability

All data used in this publication are freely available on the Canada-Alberta Oil Sands Environmental Monitoring Information Portal: https://www.canada.ca/en/environment-climate-change/services/oil-sands-monitoring/monitoring-air-quality-alberta-oil-sands.html

Acknowledgements:

The authors thank the National Research Council of Canada flight crew of the Convair-580, the Air Quality Research Division technical support staff, and Stewart Cober for the management of the study. The project was funded by the Air Quality program of Environment and Climate Change Canada and the Oil Sands Monitoring (OSM) program. It is independent of any position of the OSM program.

The authors declare no competing interests.